NF-κB-Inducing Kinase (NIK) Governs the Mitochondrial Respiratory Capacity, Differentiation, and Inflammatory Status of Innate Immune Cells

Authors: Justin N. Keeney[1], Ashley Winters[2], Raquel Sitcheran[1]*, A. Phillip West[2]*

[1]Department of Molecular & Cellular Medicine & [2]Department of Microbial Pathogenesis and Immunology, School of Medicine, Texas A&M University, Bryan, TX, USA

Running Title: NIK controls metabolism and function of innate immune cells.

Funding: This work was supported by NIH grants R01HL148153 to A.P.W. and R01NS082554 R.S. Additional support was provided by the Texas A&M University Office of the Vice President for Research via an X-Grant to A.P.W. and R.S.

* **Correspondence**: Address correspondence and reprint requests to Dr. Raquel Sitcheran (sitcheran@tamu.edu) or Dr. A. Phillip West (awest@tamu.edu).

Keywords: NIK, macrophage, myeloid cells, innate immunity, mitochondria, oxidative metabolism, inflammation

Abstract

NF-κB-Inducing Kinase (NIK), which is essential for the activation of the noncanonical NF-κB pathway, regulates diverse processes in immunity, development, and disease. While recent work has elucidated important functions for NIK in adaptive immune cell and cancer cell metabolism, roles for NIK in metabolic-driven inflammatory responses in innate immune cells remain unclear. Here we demonstrate that NIK-deficient bone marrow-derived macrophages exhibit defects in mitochondrial-dependent metabolism and oxidative phosphorylation (OXPHOS) functions that impair acquisition of a pro-repair, anti-inflammatory phenotype. Subsequently, NIK-deficient mice exhibit skewing of myeloid cells characterized by aberrant eosinophil, monocyte, and macrophage cell populations in the blood, bone marrow, and adipose tissue. Furthermore, NIK-deficient blood monocytes display hyperresponsiveness to bacterial lipopolysaccharide and elevated TNFα production ex vivo, indicative of systemic inflammation. These findings suggest that NIK is required for the metabolic rewiring of mitochondrial respiration that is critical for balancing pro- and anti-inflammatory myeloid immune cell functions. Overall, our work highlights a previously unrecognized role for NIK as a molecular rheostat that fine-tunes immunometabolism in innate immunity and suggests that metabolic dysfunction may be an important driver of inflammatory diseases caused by aberrant NIK expression or activity.

Introduction

Macrophages are an important component of the innate immune system with roles in immunity, tissue homeostasis, and cancer (1). In vivo, macrophages exist across a spectrum of polarization states and can adopt pro-inflammatory or anti-inflammatory properties depending on local cytokine gradients and tissue residency (2). Murine macrophages derived from bone marrow-derived precursors (BMDMs) can be polarized toward the extreme end of the pro-inflammatory spectrum by culture in bacterial lipopolysaccharide (LPS) or interferon gamma. These so-called M1 or M(LPS) macrophages produce pro-inflammatory cytokines such as TNFα, have bactericidal and phagocytic functionality, and can produce reactive oxygen species (ROS) and nitric oxide (NO) (3). Conversely, culture of BMDMs in interleukin-4 (IL-4) skews toward the anti-inflammatory end of the spectrum. These so-called M2 or M(IL-4) macrophages can dampen inflammatory responses by secreting anti-inflammatory cytokines such as interleukin-10 (IL-10), can promote extracellular matrix remodeling, and can enhance stromal cell proliferation (3). It is well appreciated that metabolic switches promote the acquisition of distinct polarization states and play pivotal roles in the final effector cell functionality (4). M1 macrophages upregulate glycolysis, have a broken tricarboxylic acid (TCA) cycle, and display impaired oxidative phosphorylation (OXPHOS), leading to enhanced generation of TCA intermediates such as succinate and other metabolites necessary for ROS and NO generation (5–7). On the other hand, M2 macrophages have an intact TCA cycle and upregulate OXPHOS and fatty acid oxidation in order to generate anti-inflammatory products such as glucocorticoids, IL-10, IL-13, etc. (8, 9). These metabolic shifts are critical for macrophage function, as small molecules that inhibit the major metabolic enzymes in glycolysis, TCA, and OXPHOS can dramatically alter polarization states in vitro and in vivo (10–12).

Nuclear factor-kappaB (NF-κB) signaling has a well-established role in inflammatory processes with the canonical NF-κB pathway rapidly responding to inflammatory stimuli (13). Alternatively the non-canonical NF-κB pathway, which requires NF-κB Inducing Kinase (NIK; also known as MAP3K14), regulates immune cell differentiation, development, and tissue homeostasis (13–16). Over the last decade, NIK has been found to play many novel roles in a diverse set of immune cells and their progenitors (17, 18). Within the bone marrow, NIK promotes mitochondrial biogenesis during osteoclastogenesis (14). In microglia, the tissue resident macrophage of the brain, NIK is important for the induction of cytokine expression which aids in T cell recruitment in an animal model of experimental autoimmune encephalomyelitis (19, 20).

Recently, we and others have demonstrated roles for NIK in regulating mitochondrial function and metabolism in cancer cells (19, 21–23). For example, we reported that NIK regulates mitochondrial dynamics (21) and promotes oxidative metabolism (22) in glioblastoma – an aggressive form of brain cancer. Moreover, NIK deficient glioblastoma cells exhibit impaired mitochondrial fission along with increased glycolysis to compensate for a diminished oxidative metabolism (21, 22) and are less invasive. Notably, we have shown that these novel metabolic roles for NIK are largely independent of non-canonical NF-κB signaling, suggesting direct roles for NIK in regulating mitochondrial function. Another recent study has shown that NIK shapes metabolism of CD8 T cells independently of non-canonical NF-κB by stabilizing hexokinase 2 and promoting NADPH generation (23). Although NIK has emerged as a key regulator of tumor cell and lymphocyte metabolism, whether NIK regulates immunometabolic switches in myeloid innate immune cells remains unclear.

Studies using NIK knockout (NIK KO) mice have revealed that NIK deficiency promotes a dramatic increase in eosinophils in the peripheral blood (24). NIK KO mice develop a hypereosinophilic inflammatory disease that is driven by infiltration pathogenic eosinophilic granulocytes into diverse organs, including skin, liver, lung, and esophagus, leading to early death (24, 25). Recent work has shown that eosinophils upregulate OXPHOS upon activation (26); however, it remains unclear whether immunometabolic switches contribute to the inflammatory myeloid phenotypes observed in NIK KO mice. To begin to address this knowledge gap, we measured mitochondrial and metabolic parameters in BMDMs from NIK KO mice. Here, we show that NIK promotes oxidative metabolism in macrophages, and that loss of NIK results in hyperinflammatory myeloid skewing of the bone marrow, blood, and other tissues. Our findings demonstrate that NIK is an important molecular rheostat that maintains mitochondrial function to control innate immune cell function, and they suggest that metabolic alterations may contribute to diseases where NIK activity is downregulated or lost.

Results

NIK regulates oxidative metabolism in macrophages by controlling mitochondrial respiratory capacity and OXPHOS complex activity.

To investigate how NIK regulates innate immune cell function, we examined metabolic shifts during polarization of bone marrow derived macrophages (BMDMs) from wild-type (WT) and NIK knockout (NIK KO) mice. After differentiation in M-CSF for 7 days, we noted that M0 macrophages from NIK KO mice displayed reduced basal and maximal oxygen consumption (OCR) rates, as well as impaired mitochondrial spare respiratory capacity (SRC) (**Figure 1A**).

Upon treatment with Interleukin-4 (IL-4) to stimulate an M2-like phenotype (M(IL-4)), NIK KO BMDMs were unable to increase basal and maximal OCR or SRC, indicating a profound and persistent defect in oxidative metabolism (**Figure 1B**). Decreased maximal OCR and SRC were also observed in M0 and M(IL-4) treated human monocytic U937 cells after differentiation into macrophages (**Figure 1C-E**). Taken together, these data indicate that NIK regulates oxidative metabolism through the control of OXPHOS and SRC.

To gain insight into the underlying in OXPHOS deficit in NIK KO BMDMs, we performed RNA sequencing on M0 and M(IL-4) skewed BMDMs. We did not observe significant changes in expression of genes involved in glycolysis, TCA cycle, pentose phosphate pathway, glucose transporters, or the electron transport chain subunits (**Supplemental Figure 1**), indicating that loss of respiratory capacity in NIK KO BMDMs occurs at a post-transcriptional level. However, we did note a significant increase in mitochondrial superoxide production in both M0 and M(IL-4) NIK KO BMDMs compared to WTs (**Figure 2A,B**), indicating enhanced electron escape from inefficient respiratory complexes. Mitochondrial reactive oxygen species (mROS) can be produced from OXPHOS complexes I, II, and III, so we next performed enzymatic assays with isolated mitochondria to assess respiratory complex efficiency. Consistent with our mROS data, we observed that NIK KO BMDMs exhibited impaired activity of Complexes I and II compared to WT BMDMs (**Figure 2C,D**). This apparent electron transport chain defect correlated with defects in other markers of mitochondrial fitness, including increased numbers of mitochondria in the NIK KO BMDMs with reduced membrane potential (**Supplemental Figure 2A-C**) and a trend toward increased mitochondrial size (**Supplemental Figure 2D-F**). Complexes III-V exhibited no changes in activity between WT and NIK KO, regardless of the treatment of IL-4 (**Figure 2E-G**). These data suggest that NIK regulates

oxidative metabolism by promoting electron transport chain function through OXPHOS Complexes I and II.

NIK KO Macrophages Fail to Polarize to an M(IL-4) Phenotype *in vitro* and *in vivo*.

To investigate the downstream pathways impacted by the dysregulated metabolism observed in the absence of NIK, we performed RNA-sequencing of WT and NIK KO BMDMs, and evaluated transcriptional changes in macrophage phenotype signatures. We observed that there were significant defects in M2-related wound healing gene signatures in the NIK KO BMDMs compared to WT in response to IL-4 treatment (**Figure 3A**). The RNA-sequencing data was verified via qPCR for changes in expression of typical IL-4 response genes, such as Arginase 1 (Arg1) and CD163, and a significant decrease in expression was observed in Arg1 in the NIK KO BMDMs compared to WT (**Figure 3B**). Consistent with this finding, we observed a significant decrease in IL-10 secretion to the cell culture media in response to IL-4 treatment (**Figure 3C**). Additionally, after IL-4 treatment, we observed that NIK KO BMDMs harbored functional defects in migration and adhesion (**Figure 3D,E**), although phagocytic capabilities remained intact (**Figure 3F**). Taken together with the metabolic findings discussed above, these the data suggest that NIK KO BMDMs fail to fully polarize into an M(IL-4) phenotype due to a deficiency in OXPHOS activity.

Eosinophils have been shown to secrete IL-4 and promote an M(IL-4) macrophage phenotype *in vivo* (27–30). Increased peripheral and tissue eosinophil numbers have been previously described in NIK KO mice and are associated with dermatitis and esophageal eosinophilia (24, 25). Because little is known about the role of NIK within macrophages, we

investigated the relationship between the accumulated eosinophils and their effect on macrophage polarization in the visceral white adipose tissue (WAT) deposits, which are known to have low eosinophil numbers and high levels of macrophages, along with the small intestine, which has high eosinophil numbers and low levels of macrophages (28, 30, 31). It was previously reported that NIK KO mice have a decrease in body weight compared to WT controls, which also correlates with a decrease in fat mass and smaller adipocytes ((32)). We found NIK KO mice had a significant accumulation of lineage positive immune cells within the fat but a decrease within the small intestine (**Figure 3G,H,K,L**). Further analysis of immune cells in NIK KO tissues revealed a significant increase in macrophage numbers in the WAT but no change in the small intestine compared to WT littermates (**Figure 3I,M**). Interestingly, eosinophils followed a similar trend where there were higher levels in the WAT and a low amount in the small intestine (**Figure 3J,N**), suggesting persistent inflammation within the fat due to high levels of macrophages and eosinophils.

NIK KO Mice Have Increased Levels of Pro-Inflammatory Myeloid Cells in both the Blood and Bone Marrow.

Given the changes in immune populations observed in the WAT and small intestine in NIK KO mice, we performed high dimensional multiparameter flow cytometry and standard gating to phenotype circulating immune cell populations. Consistent with prior findings and roles for NIK in B cell development and function, we observed markedly reduced CD19+ B lymphocytes, but not CD3+ T cells, in the blood of NIK KO mice (**Figure 4A-B**). We also observed a large increase in the percentage of CD11b+ myeloid cells, which was characterized by a shift from neutrophils to eosinophils and Ly6C^{hi} inflammatory monocytes (**Figure 4C-F**).

Next, using t-Distributed Stochastic Neighbor Embedding (tSNE) analysis to investigate myeloid immune marker expression more broadly, we confirmed that NIK KO mice contain dramatically more inflammatory eosinophils (**Figure H, green dashed line**) (24, 25). These myeloid cells were characterized as side scatter high (SSC-A), CD11b+, Ly6C+, Ly6G^{lo}, F4-80+, and high expression of TNFα at rest (**Figure 4G-I**). We also observed that NIK KO mice possess elevated TNFα+, Ly6C^{hi} inflammatory monocytes in the blood at rest (**Figure 4G-I, black dashed line**). Ex vivo LPS stimulation of blood leukocytes revealed a greater enhancement of CD11b+ Ly6C^{hi} inflammatory monocytes in NIK KO mice compared to WT (**Figure 4J**). Four hours after LPS stimulation, CD11b+ Ly6C^{hi} monocytes from NIK KO mice produced very high levels of intracellular TNFα relative to WT monocytes **(Figure 4J,K).** Overall, these results revealed that NIK KO mice have a significant increase in blood myeloid cells that are both basally producing pro-inflammatory cytokines and hyper-responsive to innate immune stimuli , suggesting unresolved systemic inflammation.

Given the role that NIK plays a role in hemopoietic stem cell differentiation (17, 18), we next investigated the bone marrow of NIK KO mice for defects in immune populations. We found that NIK KO mice have a significant increase in the total number of bone marrow cells (**Figure 5A**), which are primarily derived from increased CD45+ lineage positive cells (**Figure 5B,C**). Analysis of CD45+ cells showed a significant increase in granulocytes in the NIK KO mice (**Figure 4D**), and specifically, eosinophils but not neutrophils (**Figure 5H,I**). Consistent with our blood findings, monocytic cells were slightly elevated (**Figure F,J**), and we observed a decrease in lymphocytes and blast cell populations (**Figure 4E,G,K,L**). These data suggest that dysregulated terminal differentiation of cell populations in circulation and the bone marrow stem from an enrichment of low proliferative cells within the stem cell niche of the bone marrow in

NIK KO mice (**Supplemental Figure 3**). Taken together, our findings demonstrate that NIK KO mice exhibit a systemic skewing toward myeloid and pro-inflammatory phenotypes in the bone marrow, circulation, and peripheral tissues, driven at least in part by dysregulated mitochondrial homeostasis and oxidative metabolism (**Figure 5M,N**).

Discussion

Although prior studies have established a critical role for NIK in controlling adaptive immunity and development, much less is known about whether and how NIK regulates innate immune functions. Similarly, while we have demonstrated that NIK acts as a stress sensor to regulate both basal and stress-induced mitochondrial metabolism to promote glioblastoma pathogenesis, it was not clear whether NIK played similar roles in non-cancerous immune cells. In this study, we identify a previously unreported requirement for NIK in regulating immunometabolic switches in myeloid cells to promote their acquisition of pro-repair and anti-inflammatory immune phenotypes. Specifically, we observed that BMDMs isolated from NIK KO mice exhibited impaired OXPHOS and the inability to fully acquire an M(IL-4) polarization state, as seen by their failure to induce M2 markers (see **Figure 3**). On a systemic level, NIK KO mice exhibit a skewing toward pro-inflammatory myeloid phenotypes in the bone marrow, blood, and adipose tissue, characterized by increased numbers of macrophages, eosinophils, and monocytes expressing high levels of TNFα. Our findings are the first to demonstrate a requirement for NIK in myeloid cell mitochondrial metabolism and macrophage polarization through regulation of electron transport chain function. Moreover, while we have observed that NIK KO bone marrow is depleted of CD45+ B lineage cells, as previously reported (33), we demonstrate a significant increase in eosinophils and CD11b+, Ly6C^{hi} monocytes expressing

elevated TNFα at baseline and after LPS challenge. These findings suggest that previously reported hyper-eosinophilia and dermatitis in NIK KO mice are associated with an inability of eosinophils to induce OXPHOS in macrophages to resolve inflammation (24, 25). Interestingly, development of eosinophilia in NIK KO mice is independent of IKK/NF-κB (34), which is consistent with our findings suggesting that the regulation of macrophage mitochondrial metabolism and TCA complex activity does not occur on a transcriptional level, as we failed to observe dramatic alterations in mitochondrial or macrophage gene expression in NIK KO BMDMs. These findings are consistent with studies in GBM cells, which demonstrate IKK/NF-kB-independent, NIK control of oxidative metabolism, mitochondrial spare respiratory capacity, and mitochondrial dynamics (21, 22), as well as glycolytic metabolism in T cells (23).

The most prominent reported phenotypes of NIK KO mice, as well as mice harboring a spontaneous *NIK* mutation ($NIK^{aly/aly}$), are their lack of lymph nodes and Peyer's patches, aberrant splenic and thymic architecture, leading to profound defects in adaptive immunity and increased susceptibility to infection (15, 35, 36). Primary Immunodeficiency Disease (PID) patients who harbor loss-of-function mutations in *NIK* have remarkably similar clinical manifestations to NIK-deficient mice, including lymphopenia, abnormal splenic architecture, and markedly reduced immunoglobulin levels leading to recurrent infections (15, 35–38). As such, PID resulting from NIK mutation has been largely attributed to aberrant NF-κB transcriptional regulatory activity leading to adaptive immunodeficiency. How loss of NIK function alters innate immune cell development and function in patients with PID is unclear, and the impact of NIK dysregulation on immunometabolic homeostasis in PID has not been previously considered. We have recently observed that NIK KO mice exhibit altered systemic metabolism characterized by an increase in aerobic glycolysis and impaired respiration (32), which is similar to patients

with primary mitochondrial diseases (MD) caused by mutations in OXPHOS genes. Patients with MD often experience recurrent infections and display adaptive immunodeficiency (39, 40), paralleling those with NIK PIDs. We and others have found that mouse models of human mitochondrial disease display pronounced myeloid skewing in the bone marrow and blood, characterized by high levels of inflammatory neutrophils and monocytes (41, 42). Moreover, we observed that the Polymerase gamma (POLG) 'mutator' model of mitochondrial DNA disease exhibits OXPHOS deficits and a switch to glycolytic metabolism, which drive enhanced pro-inflammatory phenotypes, macrophage polarization, and tissue damage (42). Myeloid phenotypes in these mitochondrial mutant mice resemble findings here with NIK KO mice. Taken together, these findings suggest that mitochondrial and metabolic dysfunction leading to innate immune rewiring could be a common feature of patients with NIK-deficient PID, Leigh Syndrome or other primary mitochondrial diseases. Future research is warranted to more thoroughly investigate these emerging links.

In conclusion, our work highlights a previously unrecognized role for NIK as a molecular rheostat that shapes the metabolic status, differentiation, and inflammatory phenotypes of myeloid cells in vitro and in vivo. Our work implicates NIK as a key factor governing innate immune cell mitochondrial function and suggests that metabolic dysfunction may be an important contributor to inflammatory and/or immunodeficiency diseases caused by aberrant NIK expression or activity. Our findings have important implications for human disease, as the bioenergetic pathways underlying immune cell phenotype and function are increasingly recognized as important nodes for therapeutic intervention in immune and inflammatory disorders. Moreover, our results provide a strong rationale for future analysis of overlapping phenotypes in inborn errors of immunity and inborn errors of metabolism, and suggest that

strategies aimed at boosting mitochondrial function may help rebalance the immune system in primary immunodeficiency caused by NIK loss of function.

Materials and methods

Mice

All animal experiments were done in accordance with animal use protocols with approved IACUC guidelines at Texas A&M University. *Map3k14* mice were purchased from Jackson lab (B6N.129-Map3k14tm1Rds/J) and maintained by heterozygous breeding. Male and female mice were used for all experiments and animal numbers are described in the figure legend.

Reagents

A comprehensive list of the antibodies, reagents, and primers can be found in Supplemental Tables 1-3, respectively.

Flow Cytometry

Circulatory and spleen immune phenotyping: The whole mouse blood was collected in sodium heparin tubes. Spleens were collected and sieved through a 100uM cell strainer. RBCs were lysed twice with ACK lysis buffer, and leukocytes were subjected to LPS stimulation (1 μg/ml) in the presence of brefeldin A and monensin for 4 hours. Fc receptors were blocked with anti-mouse CD16/CD32 (2.4G2) antibody, and cells were stained with antibodies against surface proteins, permeabilized with Foxp3/Transcription Factor Staining Buffer Kit (TNB-0607-KIT, Tonbo Biosciences, San Diego, CA, USA), and stained with antibodies against intracellular

proteins. Cells were analyzed with a Cytek Aurora 5L Spectral Analyzer. The results were plotted and analyzed using FlowJo software (BD Bioscience; Franklin Lakes, NJ, USA).

Bone marrow phenotyping: Cells were isolated from the tibia and femurs of mice as described in the bone marrow differentiation section below. After an ACK lysis step, 500k cells per mouse were taken for immune cell phenotyping and 1 million cells were stained for the stem cell analysis. Cells were stained in a 96 well plate with Live/Dead Fix Violet (eBioscience, Waltham, MA, USA) at 4°C for 20 minutes. After being washed thoroughly, cells were blocked with FC blocker (eBioscience, Waltham, MA, USA) for 10 minutes at 4°C before the addition of the primary antibody cocktail which incubated with the cells for 30 minutes. After, cells were washed and fixed with 4% paraformaldehyde for 10 minutes at room temperature in the dark. Flow cytometric analysis was performed on a BD Fortessa X-20 (BD Bioscience; Franklin Lakes, NJ, USA). The results were plotted and analyzed using FlowJo software (BD Bioscience; Franklin Lakes, NJ, USA).

Fat and small intestine immune phenotyping: Visceral fat deposits and a 5cm section of the ileum were harvested from mice and washed with PBS before being placed in a 0.2% (2mg/mL) collagenase 2 solution, (Worthington Biochemical; Lakewood, NJ, USA) diluted in RIPA buffer (Gibco, ThermoFisher Scientific; Waltham, MA, USA), under contestant stirring for 60 minutes at 37°C. The isolated cells were filtered through a 70 μM cell strainer and red blood cells were lysed with ACK lysis buffer (VWR; Radnor, PA, USA). Cells were then stained as described above for the bone marrow.

Mitochondrial flow cytometry assays: This assay was previously described (43), but in brief: WT and NIK KO BMDMs were treated with 20ng/mL IL-4 for 5 hours before cells were detached using PBS containing 1mM EDTA (Gibco, ThermoFisher Scientific; Waltham, MA, USA). Cells were then stained with a combination of Mitotracker Green FM, Mitotracker Red FM, Mitosox, Anti-MO CD11b, and Violet live dead dye for 15 minutes in a 37°C tissue culture incubator. Cells were then washed twice before analysis on the BD Fortessa X-20 flow cytometer. The results were plotted and analyzed using FlowJo software (BD Bioscience; Franklin Lakes, NJ, USA).

Cell Culture

L929 and HEK293T cells were obtained from the American Type Culture Collection (ATCC) and maintained in Dulbecco's Modified Eagle's Medium (DMEM; Gibco, ThermoFisher Scientific; Waltham, MA, USA) supplemented with 10% fetal bovine serum (FBS; VWR; Radnor, PA, USA). BMDMs were generated by crushing the tibia and tibias of unpooled mice with red blood cells being lysed with ACK lysis buffer (VWR; Radnor, PA, USA) followed by filtering through a 40 μM cell strainer. Cells were then cultured on petri plates in DMEM containing 10% FBS and 30% L929 cultured media for 7 days with fresh media being added on day 4 post plating. IL-4 (PeproTech; Rocky Hill, NJ, USA) was used at a concentration of 20ng/mL for *in vitro* experiments unless otherwise stated. Human U937 monocytic cells were a gift from Dr. Kristen Patrick and maintained in Roswell Park Memorial Institute 1640 Medium (RPMI 1640; Gibco, ThermoFisher Scientific, Waltham, MA, USA) supplemented with 10% FBS. To differentiate U937 monocytes into macrophages, cells were treated with 100ng/mL phorbol 12-myristate 13-acetate (PMA; AmBeed, Arlington Hts, IL, USA) for 48 hours. After

that time period the media was changed, and cells were treated similarly as BMBMs. All cells were cultured at 37 °C with 95% humidity and 5% CO_2.

Lentiviral production

Twenty-four micrograms of lentiviral plasmids and 72 µg of polyethyleneimine were used to transfect HEK293T cells. After 3 days of transfection, viral supernatant was harvested and filtered through a 0.45-µM syringe filter. After filtration, viral particles were concentrated 20-fold to 400 µl using Lenti-X Concentrator (Clontech, #631231, Mountain View, CA), and 100 µl of concentrated virus was used to infect cells. 1ug/mL Puromycin (InvivoGen; San Diego, CA, USA) was used for selection until no non-transduced cells were alive.

CRISPR-Cas9 gene knockout

U937 cells were transduced with a mixture of Lenti-CrispR-v2 virus' carrying three gRNAs for each target. The gRNA sequences for human NIK were previously described (20, 21). Loss of NIK was confirmed by immunoblot of puromycin-resistant cells. Single colony cells were isolated by serial dilution. All experiments were repeated with at least three knockdown clones

Seahorse Extracellular Flux Analysis

The Seahorse XFe96 Analyzer (Agilent; Santa Clara, CA, USA) was used to measure mitochondrial respiration and glycolysis. 5 x 10^4 cells were plated per well in at least triplicate in 100µL of DMEM media containing 10%FBS in an Agilent Seahorse XF96 Cell Culture Microplate. After allowing the cells to settle at room temperature for one hour, cells were moved to a 37°C incubator for 3 hours until stimulated overnight with 20ng/mL IL-4. After 16 hours the

cells were washed and replaced with XF assay medium (Base Medium Minimal DMEM supplemented with 200mM L-glutamine pH 7.4) and incubated with a 37°C incubator without CO2 for an hour before analysis. The Oxygen Consumption Rate (OCR) was measured after sequential addition of 25 mM glucose, 1.5 μM Oligomycin A (Sigma Aldrich; Saint Louis, MO, USA), 1.5 μM FCCP (Sigma Aldrich; Saint Louis, MO, USA) plus 1 mM Sodium Pyruvate (Gibco, ThermoFisher Scientific; Waltham, MA, USA), and 2.5 μM Antimycin A (Sigma Aldrich; Saint Louis, MO, USA) plus 1.25 μM Rotenone (Enzo Life Sciences, Farmingdale, NY, USA) following a previously published protocol (44).

RNA Sequencing

1 million WT and NIK KO BMDMs were stimulated with 20ng/mL IL-4 or PBS for 6 hours before being lifted with PBS containing 1mM EDTA (Gibco, ThermoFisher Scientific; Waltham, MA, USA). Cells were spun down and washed once with PBS before being flash frozen in liquid nitrogen. Cell pellets were shipped on dry ice to Genewiz (South Plainfield, NJ, USA) where they isolated the RNA, constructed the sequencing library, and conducted the sequencing. RNA-sequencing data was analyzed using the Salmon pipeline (version 1.4.0-gompi-2020b) on the Texas A&M High Performance Research Computing Cluster. Salmon was used to align the results to the reference genome *Mus muculus* GRCm39. The data was then processed through DESeq2 (version 1.32.0) on R Studio where the annotated gene expression files were used to determine statistically significant changes in gene expression in stimulated NIK KO BMDMs relative to stimulated WT BMDMs. Ingenuity Pathway Analysis software (IPA; QIAGEN, Germantown, MD, USA) was used to identify gene families and potential upstream regulators within the datasets. GraphPad Prism (San Diego, CA, USA) was used to make heatmaps. Raw

and analyzed RNASeq datasets will be deposited into the NCBI GEO upon acceptance of the manuscript.

Gene Expression

$5x10^5$ WT and NIK KO BMDMs were stimulated with 20ng/mL IL-4 for 6 hours before being lifted with PBS containing 1mM EDTA (Gibco, ThermoFisher Scientific; Waltham, MA, USA). Cells were spun down and washed once with PBS before total RNA was isolated from cells by Purelink™ RNA Mini Kit (Life Technologies). cDNA was synthesized from 1 μg total RNA using iScript reverse transcription supermix (Bio-Rad, Hercules, CA) following the manufacturer's protocol. Quantitative RT-PCR was performed using Universal SYBR Green Supermix with StepOnePlus Real-Time PCR System (Applied Biosystems, Foster City, CA). Data was graphed as a $2^{\Delta\Delta CT}$ fold change with the gene expression data being normalized to the house keeping gene RPS18.

Immunofluorescence

BMDMs were grown on 12mm coverslips at 6 × 105 cells/well. Cells were treated with 200ng/ml LPS for 24 hours. After washing in PBS, cells were fixed with 4% paraformaldehyde for 20 min, permeabilized with 0.1% Triton X-100 in PBS for 5 min, blocked with PBS containing 5% FBS for 30 min, stained with primary antibodies for 1 hour, and stained with secondary antibodies for 1 hour. Cells were washed with PBS containing 5% FBS between each step Coverslips were mounted with Prolong Gold anti-fade reagent containing DAPI (Molecular Probes). Cells were imaged on an Olympus FV3000 confocal laser scanning microscope using a 100X oil-immersed objective.

Mitochondrial isolation

Two million WT and NIK KO BMDMs were plated in a 6 well plate and treated as described previously. At the time of harvest, cells were washed with PBS and scraped into a 1.5mL tube before spinning down. PBS was replaced with 0.5mL isolation buffer (320mM Sucrose, 1mM EDTA, 10mM HEPES, pH 7.2 with KOH and stored at 4°C) containing protease inhibitors (ThermoFisher Scientific; Waltham, MA, USA). While on ice, cells in isolation buffer were passed through a 27-gauge needle 10 times before spinning at 700xg for 8 minutes at 4°C. Supernatant was removed and placed into a new tube and kept on ice while pellet was resuspended in 0.5mL isolation buffer with protease inhibitors before spinning at 700xg for 5 minutes at 4°C. Supernatant was removed and added with the previous supernatant, pellet contains nucleus, and the 1mL of supernatant was spun down at 17,000xg for 11 minutes at 4°C. After spinning the supernatant was placed into a new tube labeled cytoplasm and the pellet was resuspended in isolation buffer and spun down at 17,000xg for 11 minutes at 4°C. Following this last spin, the supernatant was discarded, and the mitochondrial pellet was resuspended in 40uL isolation buffer and protein concentration was measured by BCA assay using the Victor X3 microplate reader.

Electron transport chain activity assays

Electron transport chain activity assays were obtained from Cayman Chemical Company (Ann Arbor, MI, USA) and manufacturer's directions were followed with the following changes. 50uL of tube A was added to each well in the 96 well plate but activity buffer was used in place of the supplied mitochondria. We then added 5ug of mitochondrial protein (isolation described

previously) to a total volume of 20uL activity buffer per well. At this point each well should have 70uL per well before adding 30uL of tube B to start the reaction. Reactions were conducted at 25°C using an Epoch microplate reader.

ELISA

2 x10^6 WT or NIK KO BMDMs were plated in a 6 well plate and allowed to adhere overnight. The following day the cells were treated with PBS or 20ng/mL IL-4 for 24 hours. Media was then removed from the cells, spun down, and froze at -20°C until ready for analysis (cells were used for other experiments). IL-10 ELISA matched antibodies were obtained from Tonbo Biosciences (San Diego, CA, USA) and the ELISA was carried out according to the manufacturer's instructions. TMB Substrate was used to detect the peroxidase-labeled secondary antibody in the ELSIA kit (KPL, Gaithersburg, MD, USA). 100uL of undiluted media was used and ran in duplicate for each biological replicate.

Macrophage Heptotaxis Assay

This assay was described previously (45). In brief, WT and NIK KO BMDMs were stimulated with IL-4 (20ng/mL) for 24 hours before lifted with PBS containing 1mM EDTA (Gibco, ThermoFisher Scientific; Waltham, MA, USA). 75,000 DiO (ThermoFisher Scientific; Waltham, MA, USA) labeled BMDMs were plated on the insert of an 8.0μm pore, polyester membrane Transwell Permeable Support (Corning Incorporated; Corning, NY, USA) which was precoated for 3 hours at 37°C with 4ug/mL fibrinogen (Sigma-Aldrich; Saint Louis, MO, USA). After letting the cells settle for 3 hours, the media was removed and a Matrigel Matrix (50% Matrigel,

49% Culture media, 1% FBS) was added on top of the cell layer (Corning Incorporated; Corning, NY, USA). Once the Matrigel matrix solidified, a solution of 100nM N-Formyl-Met-Leu-Phe [FMLP] (Sigma-Aldrich; Saint Louis, MO, USA) was added to the top of the Matrigel to induce a chemokine gradient. Cells were allowed to migrate for 24 hours before z-stack images were acquired on a Nikon A1R Confocal microscope (Nikon Instruments; Melville, NY, USA). Images were then processed in Imaris 9.5.0 (Oxford Instruments; Abingdon, Oxfordshire, UK) before counting the number of cells invaded. Data was graphed as a fold change to WT of the number of total cells that invaded.

Macrophage Adhesion Assay

This assay was described previously (45). In brief, WT and NIK KO BMDMs were stimulated with IL-4 (20ng/mL) for 24 hours before being lifted with PBS containing 1mM EDTA (Gibco, ThermoFisher Scientific; Waltham, MA, USA). Cells were diluted to a concentration of 1 million cells/mL and 50uL of cell solution was plated on a precoated 4ug/mL fibrinogen and 0.5% polyvinyl alcohol (Sigma-Aldrich; Saint Louis, MO, USA) 96-well plate. Cells were plated with technical replicates and allowed to sit for 30 minutes in a 37˚C tissue culture incubator. Cells were then washed once with PBS before staining the adhered cells with the CyQUANT DNA stain according to the manufacturer's instructions (Invitrogen, ThermoFisher Scientific; Waltham, MA, USA). Fluorescence signal was measured on the Victor X3 microplate reader and cell number was determined through a standard curve of cells.

Macrophage Phagocytosis Assay

WT and NIK KO BMDMs were plated subconfluently in a 6-well plate before being stimulated with IL-4 (20ng/mL) for 24 hours. 10^8 1um carboxylate microspheres (Polysciences Inc; Warrington, PA, USA) were coated in a 50% mouse serum (MP Biomedicals; Irvine, CA, USA) solution and incubated for 30 minutes at 37˚C. The solution was then diluted to 5% serum before being added to cells and allowed to incubate for 2 hours. After, cells were washed twice with PBS before fixing with 4%PFA. Once the PFA was washed, cells were stained with Phalloidin and Hoechst (Invitrogen, ThermoFisher Scientific; Waltham, MA, USA) and imaged on a Nikon Eclipse Ti microscope.

Statistical Analysis

Statistical analyses were carried out using GraphPad Prism (San Diego, CA, USA), and details can be found in the figure legends where applicable. The data presented here was considered statistically significant if $p < 0.05$.

Acknowledgements

We thank Dr. Kristin Patrick for providing U937 cells.

Disclosures

The authors declare no financial conflicts of interest.

References

1. Shapouri-Moghaddam, A., S. Mohammadian, H. Vazini, M. Taghadosi, S.-A. Esmaeili, F. Mardani, B. Seifi, A. Mohammadi, J. T. Afshari, and A. Sahebkar. 2018. Macrophage plasticity, polarization, and function in health and disease. *J. Cell. Physiol.* 233: 6425–6440.

2. Murray, P. J., J. E. Allen, S. K. Biswas, E. A. Fisher, D. W. Gilroy, S. Goerdt, S. Gordon, J. A. Hamilton, L. B. Ivashkiv, T. Lawrence, M. Locati, A. Mantovani, F. O. Martinez, J.-L. Mege, D. M. Mosser, G. Natoli, J. P. Saeij, J. L. Schultze, K. A. Shirey, A. Sica, J. Suttles, I. Udalova, J. A. van Ginderachter, S. N. Vogel, and T. A. Wynn. 2014. Macrophage Activation and Polarization: Nomenclature and Experimental Guidelines. *Immunity* 41: 14–20.

3. Orecchioni, M., Y. Ghosheh, A. B. Pramod, and K. Ley. 2019. Macrophage Polarization: Different Gene Signatures in M1(LPS+) vs. Classically and M2(LPS–) vs. Alternatively Activated Macrophages. *Front. Immunol.* 10: 1–14.

4. Viola, A., F. Munari, R. Sánchez-Rodríguez, T. Scolaro, and A. Castegna. 2019. The Metabolic Signature of Macrophage Responses. *Front. Immunol.* 10: 1462.

5. Ahmed, D., D. Roy, A. Jaworski, A. Edwards, A. Abizaid, A. Kumar, A. Golshani, and E. Cassol. 2019. Differential remodeling of the electron transport chain is required to support TLR3 and TLR4 signaling and cytokine production in macrophages. *Sci. Rep.* 9: 18801.

6. Scialò, F., D. J. Fernández-Ayala, and A. Sanz. 2017. Role of Mitochondrial Reverse Electron Transport in ROS Signaling: Potential Roles in Health and Disease. *Front. Physiol.* 8: 1–7.

7. Palmieri, E. M., M. Gonzalez-Cotto, W. A. Baseler, L. C. Davies, B. Ghesquière, N. Maio, C. M. Rice, T. A. Rouault, T. Cassel, R. M. Higashi, A. N. Lane, T. W.-M. Fan, D. A. Wink, and D. W. McVicar. 2020. Nitric oxide orchestrates metabolic rewiring in M1 macrophages by targeting aconitase 2 and pyruvate dehydrogenase. *Nat. Commun.* 11: 698.

8. Zhang, Q., H. Wang, C. Mao, M. Sun, G. Dominah, L. Chen, and Z. Zhuang. 2018. Fatty acid oxidation contributes to IL-1β secretion in M2 macrophages and promotes macrophage-mediated tumor cell migration. *Mol. Immunol.* 94: 27–35.

9. Mills, E. L., and L. A. O'Neill. 2016. Reprogramming mitochondrial metabolism in macrophages as an anti-inflammatory signal. *Eur. J. Immunol.* 46: 13–21.

10. Fan, J., K. A. Krautkramer, J. L. Feldman, and J. M. Denu. 2015. Metabolic regulation of histone post-translational modifications. *ACS Chem. Biol.* 10: 95–108.

11. Rath, M., I. Müller, P. Kropf, E. I. Closs, and M. Munder. 2014. Metabolism via Arginase or Nitric Oxide Synthase: Two Competing Arginine Pathways in Macrophages. *Front. Immunol.* 5: 532.

12. Makowski, L., M. Chaib, and J. C. Rathmell. 2020. Immunometabolism: From basic mechanisms to translation. *Immunol. Rev.* 295: 5–14.

13. Pflug, K. M., and R. Sitcheran. 2020. Targeting NF-κB-Inducing Kinase (NIK) in Immunity, Inflammation, and Cancer. *Int. J. Mol. Sci.* 21: 8470.

14. Zeng, R., R. Faccio, and D. V. Novack. 2015. Alternative NF-κB Regulates RANKL-Induced Osteoclast Differentiation and Mitochondrial Biogenesis via Independent Mechanisms. *J. Bone Miner. Res. Off. J. Am. Soc. Bone Miner. Res.* 30: 2287–2299.

15. Yin, L., L. Wu, H. Wesche, C. D. Arthur, J. M. White, D. V. Goeddel, and R. D. Schreiber. 2001. Defective lymphotoxin-beta receptor-induced NF-kappaB transcriptional activity in NIK-deficient mice. *Science* 291: 2162–2165.

16. Hahn, M., A. Macht, A. Waisman, and N. Hövelmeyer. 2016. NF-κB-inducing kinase is essential for B-cell maintenance in mice. *Eur. J. Immunol.* 46: 732–741.

17. Zhao, C., Y. Xiu, J. Ashton, L. Xing, Y. Morita, C. T. Jordan, and B. F. Boyce. 2012. Noncanonical NF-κB signaling regulates hematopoietic stem cell self-renewal and microenvironment interactions. *Stem Cells Dayt. Ohio* 30: 709–718.

18. Xiu, Y., W. Y. Xue, A. Lambertz, M. Leidinger, K. Gibson-Corley, and C. Zhao. 2017. Constitutive Activation of NIK Impairs the Self-Renewal of Hematopoietic Stem/Progenitor Cells and Induces Bone Marrow Failure. *STEM CELLS* 35: 777–786.

19. Jie, Z., C.-J. Ko, H. Wang, X. Xie, Y. Li, M. Gu, L. Zhu, J.-Y. Yang, T. Gao, W. Ru, S.-J. Tang, X. Cheng, and S.-C. Sun. 2021. Microglia promote autoimmune inflammation via the noncanonical NF-κB pathway. *Sci. Adv.* 7: eabh0609.

20. Duran, C. L., D. W. Lee, J.-U. Jung, S. Ravi, C. B. Pogue, L. G. Toussaint, K. J. Bayless, and R. Sitcheran. 2016. NIK regulates MT1-MMP activity and promotes glioma cell invasion independently of the canonical NF-κB pathway. *Oncogenesis* 5: e231–e231.

21. Jung, J.-U., S. Ravi, D. W. Lee, K. McFadden, M. L. Kamradt, L. G. Toussaint, and R. Sitcheran. 2016. NIK/MAP3K14 Regulates Mitochondrial Dynamics and Trafficking to Promote Cell Invasion. *Curr. Biol.* 26: 3288–3302.

22. Kamradt, M. L., J.-U. Jung, K. M. Pflug, D. W. Lee, V. Fanniel, and R. Sitcheran. 2021. NIK promotes metabolic adaptation of glioblastoma cells to bioenergetic stress. *Cell Death Dis.* 12: 1–18.

23. Gu, M., X. Zhou, J. H. Sohn, L. Zhu, Z. Jie, J.-Y. Yang, X. Zheng, X. Xie, J. Yang, Y. Shi, H. D. Brightbill, J. B. Kim, J. Wang, X. Cheng, and S.-C. Sun. 2021. NF-κB-inducing kinase maintains T cell metabolic fitness in antitumor immunity. *Nat. Immunol.* 22: 193–204.

24. Häcker, H., L. Chi, J. E. Rehg, and V. Redecke. 2012. NF-κB-inducing kinase (NIK) prevents the development of hypereosinophilic syndrome (HES)-like disease in mice independent of IKKα activation. *J. Immunol. Baltim. Md 1950* 188: 4602–4610.

25. Eden, K., D. E. Rothschild, D. K. McDaniel, B. Heid, and I. C. Allen. 2017. Noncanonical NF-κB signaling and the essential kinase NIK modulate crucial features associated with eosinophilic esophagitis pathogenesis. *Dis. Model. Mech.* 10: 1517–1527.

26. Porter, L., N. Toepfner, K. R. Bashant, J. Guck, M. Ashcroft, N. Farahi, and E. R. Chilvers. 2018. Metabolic Profiling of Human Eosinophils. *Front. Immunol.* 9: 1404.

27. Rose, C. E., J. A. Lannigan, P. Kim, J. J. Lee, S. M. Fu, and S. J. Sung. 2010. Murine lung eosinophil activation and chemokine production in allergic airway inflammation. *Cell. Mol. Immunol.* 7: 361–374.

28. Yoon, J., H.-N. Um, J. Jang, Y.-A. Bae, W.-J. Park, H. J. Kim, M.-S. Yoon, I. Y. Chung, and Y. Jung. 2019. Eosinophil Activation by Toll-Like Receptor 4 Ligands Regulates Macrophage Polarization. *Front. Cell Dev. Biol.* 7: 329.

29. Qiu, Y., K. D. Nguyen, J. I. Odegaard, X. Cui, X. Tian, R. M. Locksley, R. D. Palmiter, and A. Chawla. 2014. Eosinophils and type 2 cytokine signaling in macrophages orchestrate development of functional beige fat. *Cell* 157: 1292–1308.

30. Wu, D., A. B. Molofsky, H.-E. Liang, R. R. Ricardo-Gonzalez, H. A. Jouihan, J. K. Bando, A. Chawla, and R. M. Locksley. 2011. Eosinophils sustain adipose alternatively activated macrophages associated with glucose homeostasis. *Science* 332: 243–247.

31. Jung, Y., and M. E. Rothenberg. 2014. Roles and Regulation of Gastrointestinal Eosinophils in Immunity and Disease. *J. Immunol. Baltim. Md 1950* 193: 999–1005.

32. Pflug, K. M., D. W. Lee, and R. Sitcheran. 2021. NF-κB-Inducing Kinase Rewires Metabolic Homeostasis and Promotes Diet-Induced Obesity. 2021.08.26.457753.

33. Brightbill, H. D., J. K. Jackman, E. Suto, H. Kennedy, C. Jones, S. Chalasani, Z. Lin, L. Tam, M. Roose-Girma, M. Balazs, C. D. Austin, W. P. Lee, and L. C. Wu. 2015. Conditional Deletion of NF-κB-Inducing Kinase (NIK) in Adult Mice Disrupts Mature B Cell Survival and Activation. *J. Immunol. Baltim. Md 1950* 195: 953–964.

34. Häcker, H., L. Chi, J. E. Rehg, and V. Redecke. 2012. NIK Prevents the Development of Hypereosinophilic Syndrome-like Disease in Mice Independent of IKKα Activation. *J. Immunol.* 188: 4602–4610.

35. Dejardin, E., N. M. Droin, M. Delhase, E. Haas, Y. Cao, C. Makris, Z.-W. Li, M. Karin, C. F. Ware, and D. R. Green. 2002. The lymphotoxin-beta receptor induces different patterns of gene expression via two NF-kappaB pathways. *Immunity* 17: 525–535.

36. Weih, F., and J. Caamaño. 2003. Regulation of secondary lymphoid organ development by the nuclear factor-kappaB signal transduction pathway. *Immunol. Rev.* 195: 91–105.

37. Schlechter, N., B. Glanzmann, E. G. Hoal, M. Schoeman, B.-S. Petersen, A. Franke, Y.-L. Lau, M. Urban, P. D. van Helden, M. M. Esser, M. Möller, and C. Kinnear. 2017. Exome Sequencing Identifies a Novel MAP3K14 Mutation in Recessive Atypical Combined Immunodeficiency. *Front. Immunol.* 8: 1624.

38. Willmann, K. L., S. Klaver, F. Doğu, E. Santos-Valente, W. Garncarz, I. Bilic, E. Mace, E. Salzer, C. Domínguez Conde, H. Sic, P. Májek, P. P. Banerjee, G. I. Vladimer, Ş. Haskoloğlu,

M. Gökalp Bolkent, A. Küpesiz, A. Condino-Neto, J. Colinge, G. Superti-Furga, W. F. Pickl, M. C. van Zelm, H. Eibel, J. S. Orange, A. Ikincioğulları, and K. Boztuğ. 2014. Biallelic loss-of-function mutation in NIK causes a primary immunodeficiency with multifaceted aberrant lymphoid immunity. *Nat. Commun.* 5: 1–13.

39. McGuire, P. J. 2019. Mitochondrial Dysfunction and the Aging Immune System. *Biology* 8: E26.

40. Kapnick, S. M., S. E. Pacheco, and P. J. McGuire. 2018. The emerging role of immune dysfunction in mitochondrial diseases as a paradigm for understanding immunometabolism. *Metabolism.* 81: 97–112.

41. Jin, Z., W. Wei, M. Yang, Y. Du, and Y. Wan. 2014. Mitochondrial Complex I Activity Suppresses Inflammation and Enhances Bone Resorption by Tipping the Balance of Macrophage-Osteoclast Polarization. *Cell Metab.* 20: 483–498.

42. Lei, Y., C. Guerra Martinez, S. Torres-Odio, S. L. Bell, C. E. Birdwell, J. D. Bryant, C. W. Tong, R. O. Watson, L. C. West, and A. P. West. 2021. Elevated type I interferon responses potentiate metabolic dysfunction, inflammation, and accelerated aging in mtDNA mutator mice. *Sci. Adv.* 7: eabe7548.

43. Monteiro, L. de B., G. G. Davanzo, C. F. de Aguiar, and P. M. M. Moraes-Vieira. 2020. Using flow cytometry for mitochondrial assays. *MethodsX* 7: 100938.

44. Van den Bossche, J., J. Baardman, and M. P. J. de Winther. 2015. Metabolic Characterization of Polarized M1 and M2 Bone Marrow-derived Macrophages Using Real-time Extracellular Flux Analysis. *J. Vis. Exp. JoVE* 1–7.

45. Cui, K., C. L. Ardell, N. P. Podolnikova, and V. P. Yakubenko. 2018. Distinct Migratory Properties of M1, M2, and Resident Macrophages Are Regulated by αDβ2 and αMβ2 Integrin-Mediated Adhesion. *Front. Immunol.* 9: 1–14.

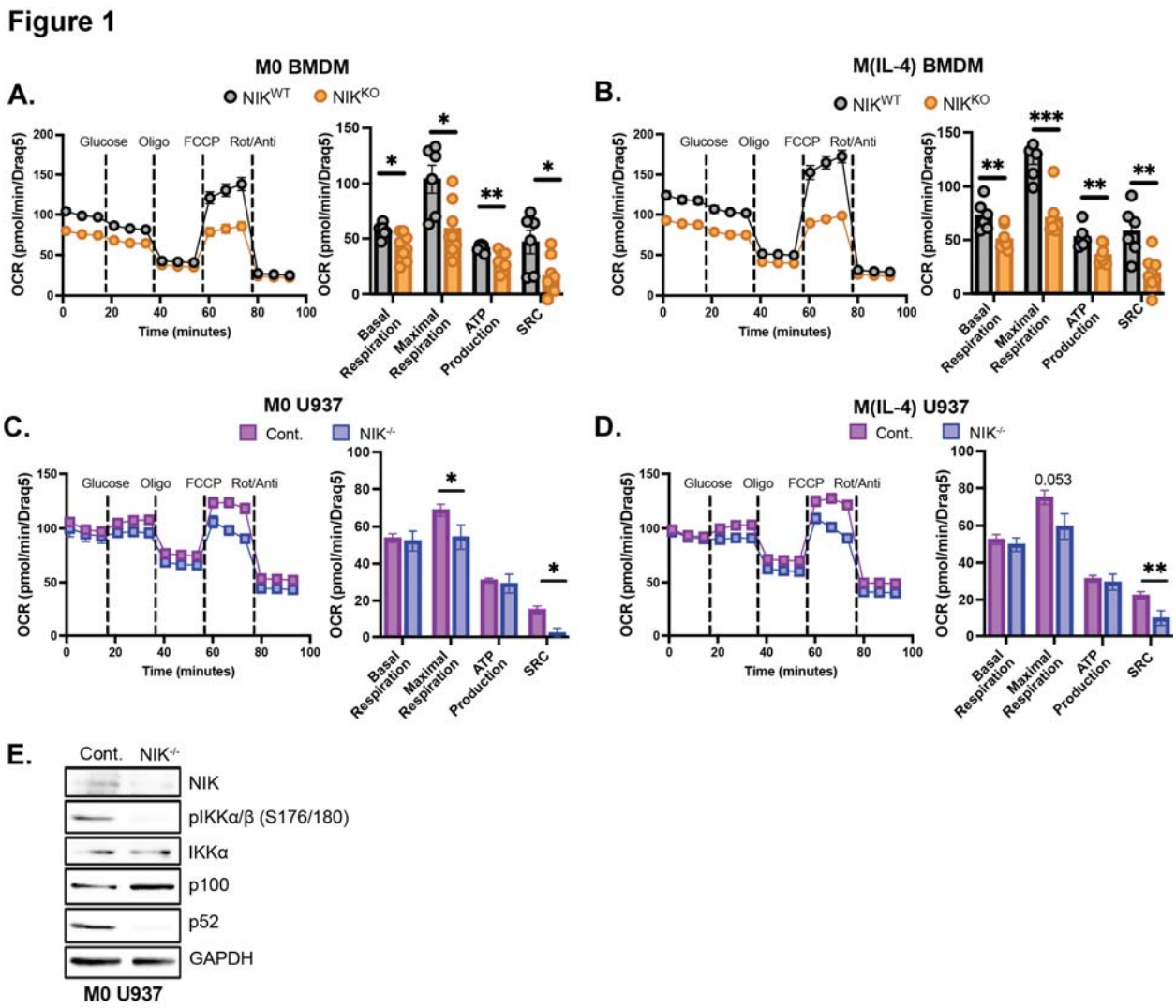

Figure 1: NIK regulates oxidative metabolism in macrophages. Seahorse extracellular flux analysis investigating changes in the oxygen consumption rate (OCR) of basal (M0) WT and NIK KO BMDMs **(A)** or after an overnight treatment with IL-4 M(IL-4) **(B)**. Line graphs are combined technical (n > 23) and biological replicates with bar graphs representing each animal (n > 6 biological replicates). Data are mean +/- SEM and statistics are a Student's T-test *p < 0.05, **p < 0.01, ***p < 0.001. Seahorse extracellular flux analysis showing **(C)** OCR readouts of basal (M0) and **(D)** IL-4 treated (M(IL-4)) WT and NIK$^{-/-}$ U937 cells. Graphs represent 3 independent experiments with treatment conditions ran in at least technical triplicates (n = 3 single cell isolated clones). Data are mean +/- SEM and statistics are a Student's T-test. *p <

0.05, **p < 0.01. **(E)** Representative western blot verifying loss of NIK in U937 cells using the empty CRISPR vector, LCV2, as a control. Samples were treated with 200ng/mL LPS and 10μM MG132 for 4 hours before extracting protein with RIPA buffer.

Figure 2

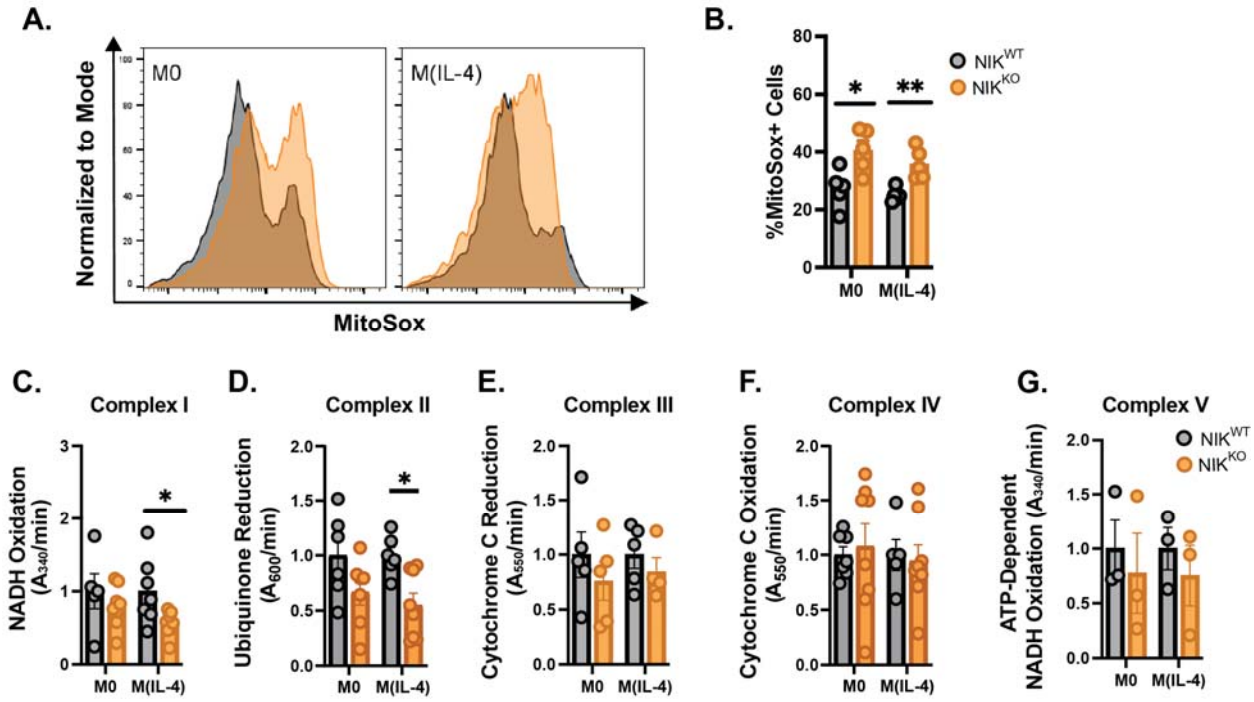

Figure 2: NIK deficient macrophages display elevated mROS and impaired OXPHOS Complex I and II activity. (A,B) Representative histograms and quantification of Mitosox levels in WT and NIK KO BMDMs post 6-hour treatment with IL-4 (n = 5 biological replicates). Statistics are a Student's T-test. *p < 0.05, **p < 0.01. Electron transport chain activity assays for Complex I **(C)**, Complex II **(D)**, Complex III **(E)**, Complex IV **(F)**, and Complex V **(G)** from basal or 24 hour IL-4 treated WT and NIK KO BMDMs. Graphs represent biological replicates (n > 3 biological replicates). Statistics are a Student's T-test. *p < 0.05.

Figure 3

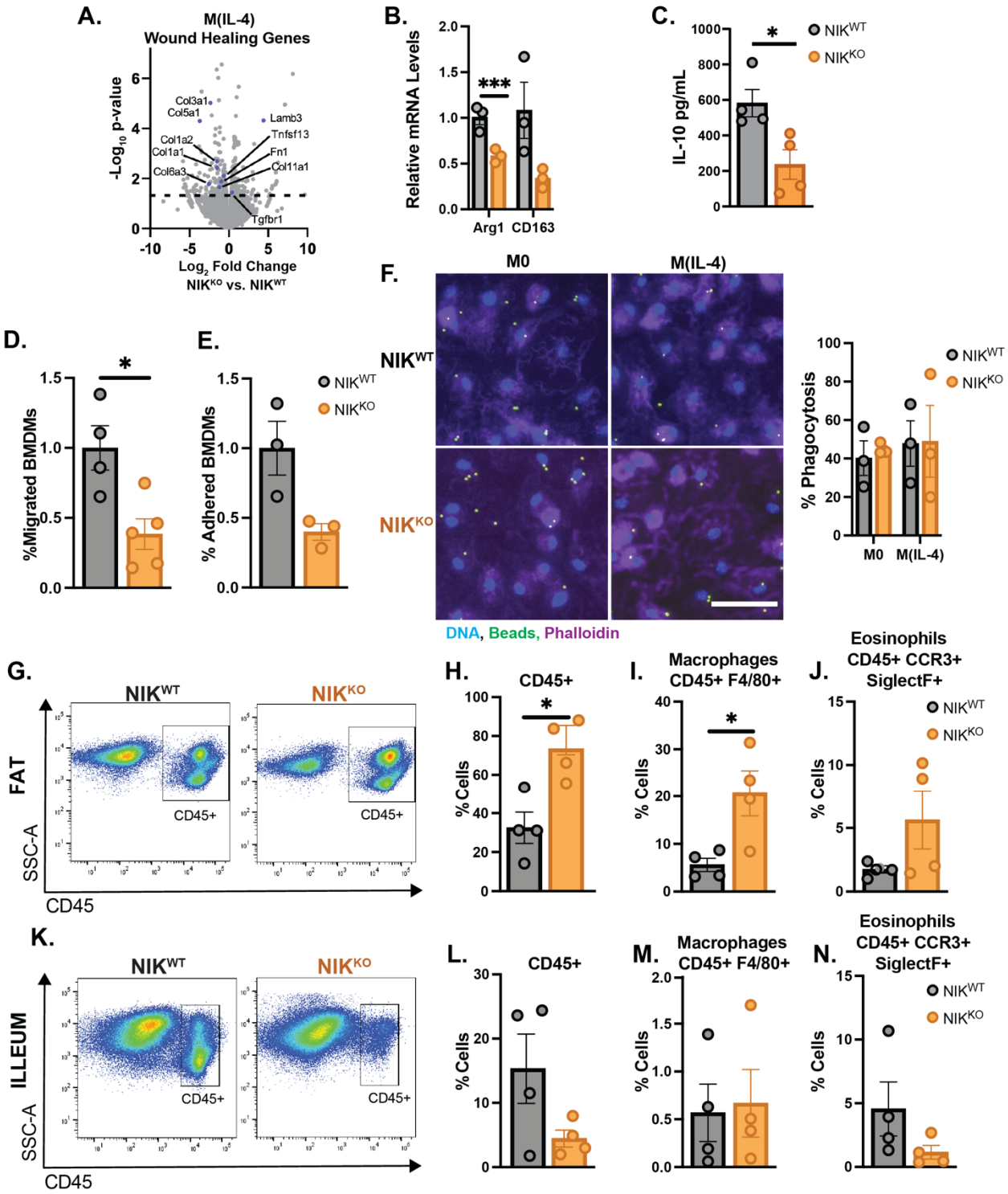

Figure 3: NIK KO macrophages fail to polarize to an M(IL-4) phenotype *in vitro* and *in vivo*. (A) RNA-sequencing data of classical pro-repair pathways in NIK KO macrophages after 6

hours of IL-4 treatment. Volcano plots represent 2 biological replicates with a Log2Fold change of NIK KO BMDMs compared back to WT. Statistics were calculated by DESeq2 and genes above the dotted line are deemed significant for having a -log(p-value) of greater than 1.3. **(B-C)** The trends in RNA-sequencing were confirmed by assessing IL-4 response genes in by RT-qPCR **(B)** and validating IL-10 levels by ELISA post 24hr IL-4 treatment in WT and NIK KO macrophages **(C)** (n > 3 biological replicates ran in triplicates). Statistics are a Student's T-test *p < 0.05, ***p < 0.001. WT and NIK KO BMDMs were stimulated for 24 hours with IL-4 before undergoing the following assays: **(D)** Cell invasion assay was performed with media containing the chemoattractant FMLP. After 24 hours invaded cells were calculated percent migrated compared to WT (n > 4 biological replicates). Statistics are a Student's T-test *p < 0.05. **(E)** Cells were plated on a PVA coated 96 well plate and allowed to settle for 30 minutes before washing with PBS and quantifying percent attached cells via CyQUANT DNA staining and comparing the NIK KO value back to WT (n = 3 biological replicates). Statistics are a Student's T-test. **(F)** Representative fluorescent images of phagocytosis assay. Graph represents % cells containing beads (n = 3 biological replicates). Statistics are a Student's T-test. *In vivo* analysis of WT and NIK KO mice investigating immune cells in the fat **(G-J)** and ileum **(K-N)** gated through single and live cells. Quantification of biological replicates analyzing total immune cells, macrophages, and eosinophils in fat (top) and ileum (bottom) is graphed as a percent of CD45+ parent gate (n = 4). Statistics are a Student's T-test. *p < 0.05.

Figure 4

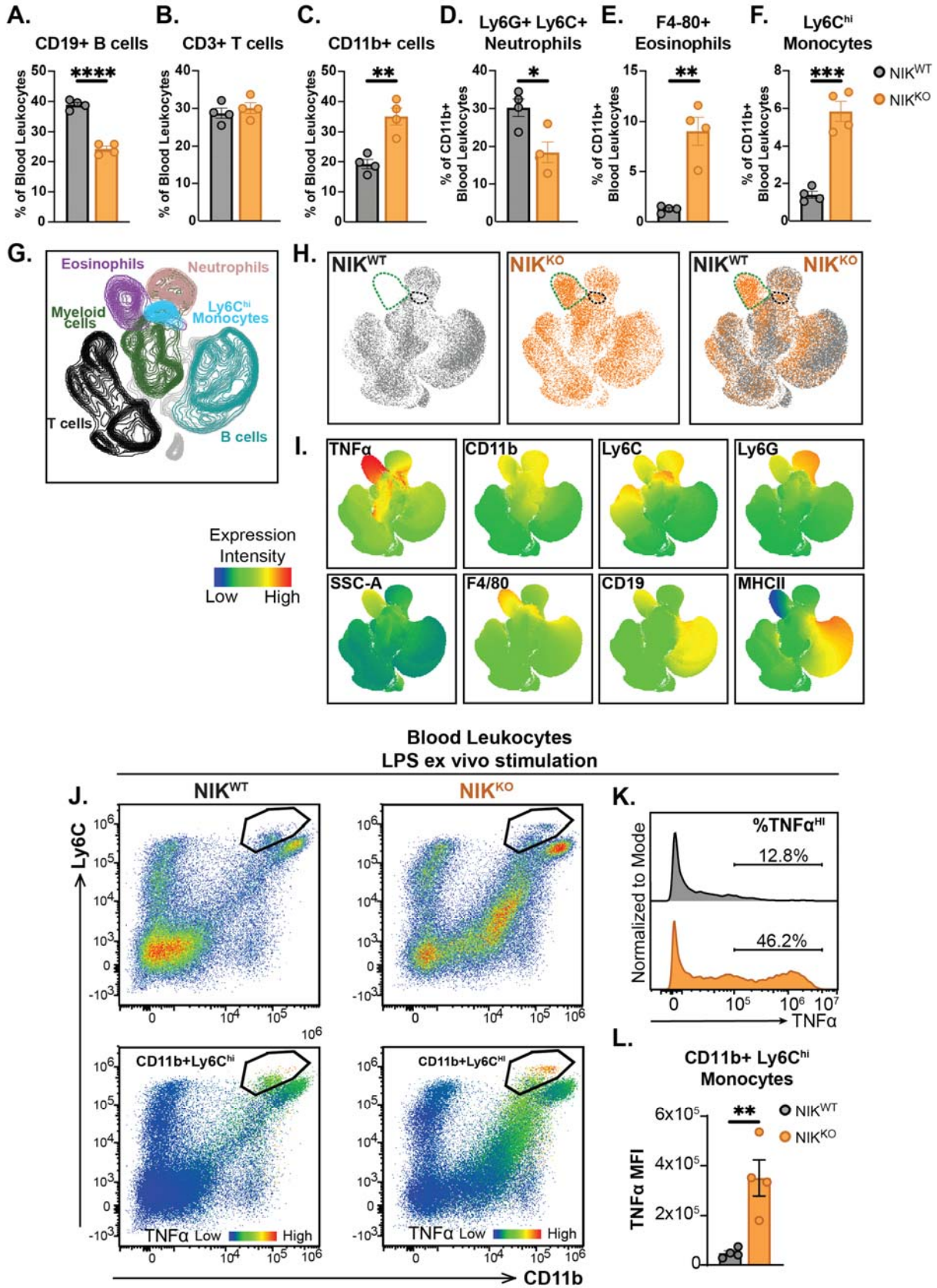
A.
CD19+ B cells
B.
CD3+ T cells
C.
CD11b+ cells
D.
Ly6G+ Ly6C+ Neutrophils
E.
F4-80+ Eosinophils
F.
Ly6C^hi Monocytes
% of Blood Leukocytes
% of CD11b+ Blood Leukocytes
****
**
*
***
NIK^WT
NIK^KO
G.
Eosinophils
Neutrophils
Myeloid cells
Ly6C^hi Monocytes
T cells
B cells
H.
NIK^WT
NIK^KO
I.
TNFα
CD11b
Ly6C
Ly6G
SSC-A
F4/80
CD19
MHCII
Expression Intensity
Low
High
Blood Leukocytes
LPS ex vivo stimulation
J.
NIK^WT
NIK^KO
Ly6C
CD11b+Ly6C^hi
TNFα Low
High
CD11b
K.
%TNFα^HI
12.8%
46.2%
Normalized to Mode
TNFα
L.
CD11b+ Ly6C^hi Monocytes
TNFα MFI

669

Figure 4: NIK KO mice exhibit increased pro-inflammatory myeloid cells in the blood at baseline and after innate immune stimulation. Blood was harvested from WT and NIK KO and subjected to red blood cell lysis with ACK buffer. Total blood leucocytes were quantified by flow cytometry using markers of B cells **(A)**, T cells **(B)**, CD11b+ myeloid cells **(C)**, neutrophils **(D)**, eosinophils **(E)**, and monocytes **(F)**. (n = 4 biological replicates). Statistics are a Student's T-test. *$p < 0.05$, **$p < 0.01$, ***$p < 0.001$, ****$p < 0.0001$. **(G-I)** T-SNE clustering of WT and NIK KO blood leukocytes representing 4 biological replicates. **(J-L)**. Blood leukocytes were stimulated with LPS ex vivo and TNFα mean fluorescence intensity (MFI) levels were quantified. Statistics are a Student's T-test. **$p < 0.01$

Figure 5

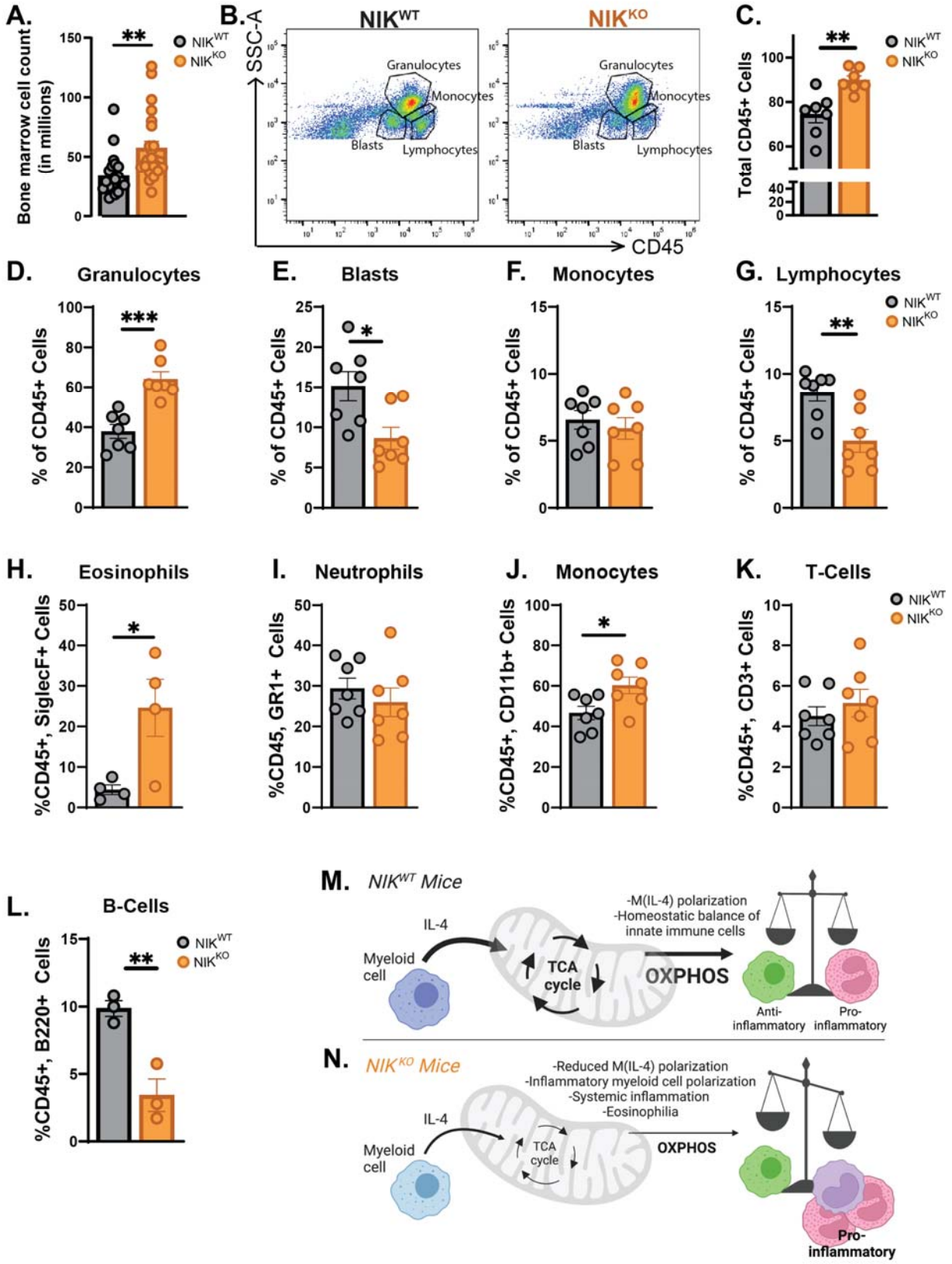
A.
Bone marrow cell count (in millions)
NIK^WT
NIK^KO
B.
NIK^WT
NIK^KO
SSC-A
CD45
Granulocytes
Monocytes
Blasts
Lymphocytes
C.
Total CD45+ Cells
D. Granulocytes
% of CD45+ Cells
E. Blasts
F. Monocytes
G. Lymphocytes
H. Eosinophils
%CD45+, SiglecF+ Cells
I. Neutrophils
%CD45, GR1+ Cells
J. Monocytes
%CD45+, CD11b+ Cells
K. T-Cells
%CD45+, CD3+ Cells
L. B-Cells
%CD45+, B220+ Cells
M. NIK^WT Mice
IL-4
Myeloid cell
TCA cycle
OXPHOS
-M(IL-4) polarization
-Homeostatic balance of innate immune cells
Anti-inflammatory
Pro-inflammatory
N. NIK^KO Mice
-Reduced M(IL-4) polarization
-Inflammatory myeloid cell polarization
-Systemic inflammation
-Eosinophilia
Pro-inflammatory

680

Figure 5: NIK KO mice exhibit myeloid skewing in the bone marrow. (A) Total bone marrow cell count after ACK red blood cell lysis (n = 23 biological replicates). Statistics are a Student's T-test **p < 0.01. **(B,C)** Quantification and flow cytometry plot of lineage positive (CD45+) cells in WT and NIK KO bone marrow (n = 7). Statistics are a Student's T-test **p < 0.01. **(D-G)** Quantification of different bone marrow cell populations in WT and NIK KO bone marrow based off of Side Scatter Area (SSC-A) and CD45 (n = 7). **(H-L)** Quantification of specific immune populations in the CD45+ parent gate utilizing indicated surface markers. Statistics are a Student's T-test and p-value is shown on the graph if the condition is not significant. *p < 0.05, **p < 0.01, ***p < 0.001. Model showing the role of NIK in WT myeloid cells promoting oxidative metabolism and having a homeostatic balance of innate immune cells **(M)** and the consequences of NIK loss resulting in decreased oxidative metabolism and systemic inflammation **(N)**.

Figure S1

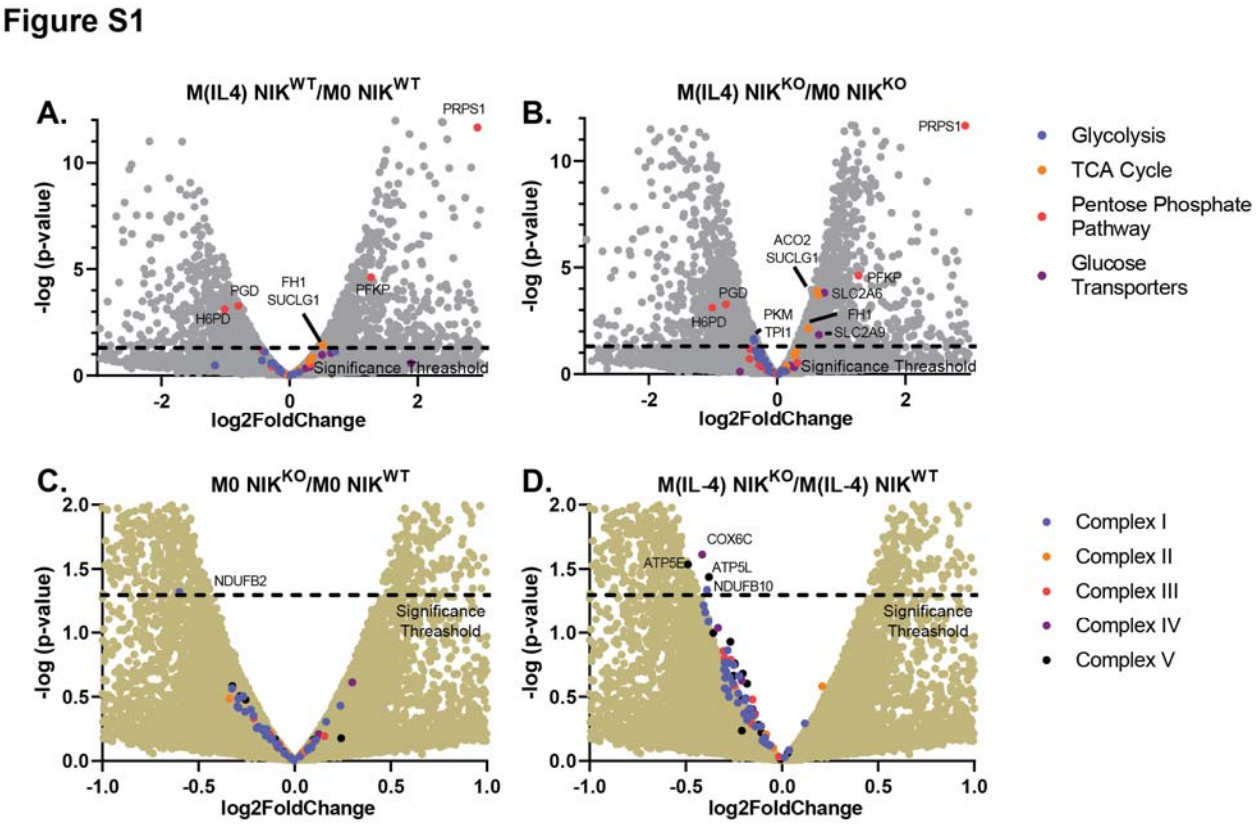

Supplemental Figure 1: NIK KO macrophages have no significant transcriptional changes in metabolic genes. RNA-sequencing heatmaps represent 2 biological replicates with a Log2Fold change post 6 hour IL-4 treatment over baseline in WT **(A)** and NIK KO BMDMs **(B)** probing for changes in genes involved in glycolysis, TCA cycle, pentose phosphate pathway, and glucose transporters. RNA-sequencing heatmaps of NIK KO macrophages compared to WT at baseline **(C)** or after 6 hour treatment of IL-4 **(D)** representing changes in gene expression of electron transport chain complex subunits. Statistics were calculated by DESeq2 and -log10 (p value) of 1.3 represents a p value of 0.05.

Figure S2

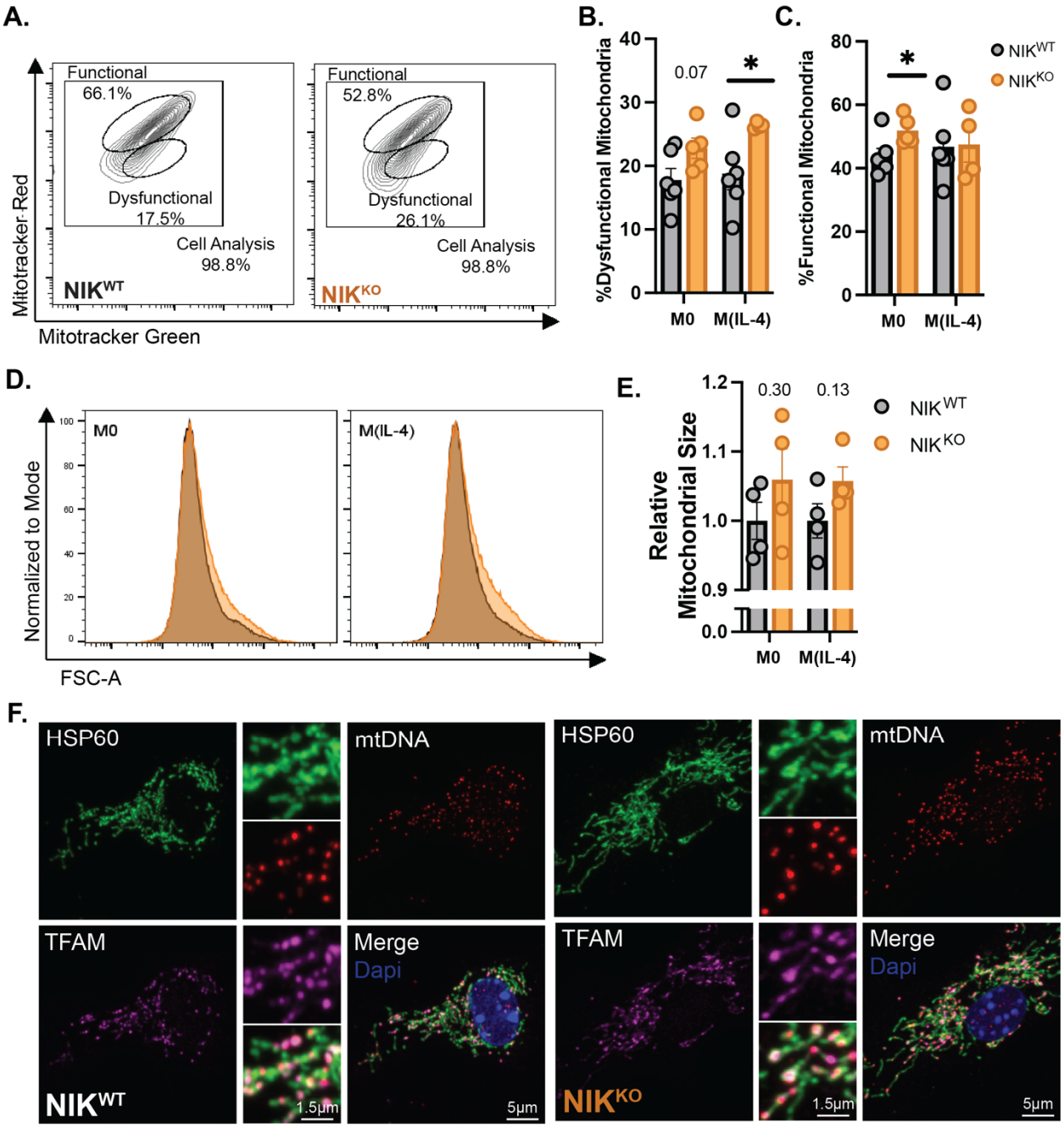

Supplemental Figure 2: Mitochondrial homeostasis is disrupted due to a loss of NIK. (A) 24 hour IL-4 stimulated BMDMs were costained with Mitotracker green and Mitotracker red to assess mitochondrial membrane potential via flow cytometry as a marker of mitochondrial functionality. Cells with high mitochondrial membrane potential were termed "functional" **(B)** and those with low membrane potential "dysfunctional" **(C)** (n = 5 biological replicates).

Statistics are a Student's T-test. *$p < 0.05$. **(D)** Isolated mitochondria were analyzed by flow cytometry against standard sized beads to calculate mitochondrial size with the quantification of mitochondrial size **(E)** (n = 4 biological replicates). Statistics are a Student's T-test. **(F)** Representative immunofluorescent images characterizing the mitochondrial network in WT and NIK KO macrophages at baseline using antibodies against HSP60 (green), mitochondrial DNA (red), TFAM (purple), and DAPI (blue).

Figure S3

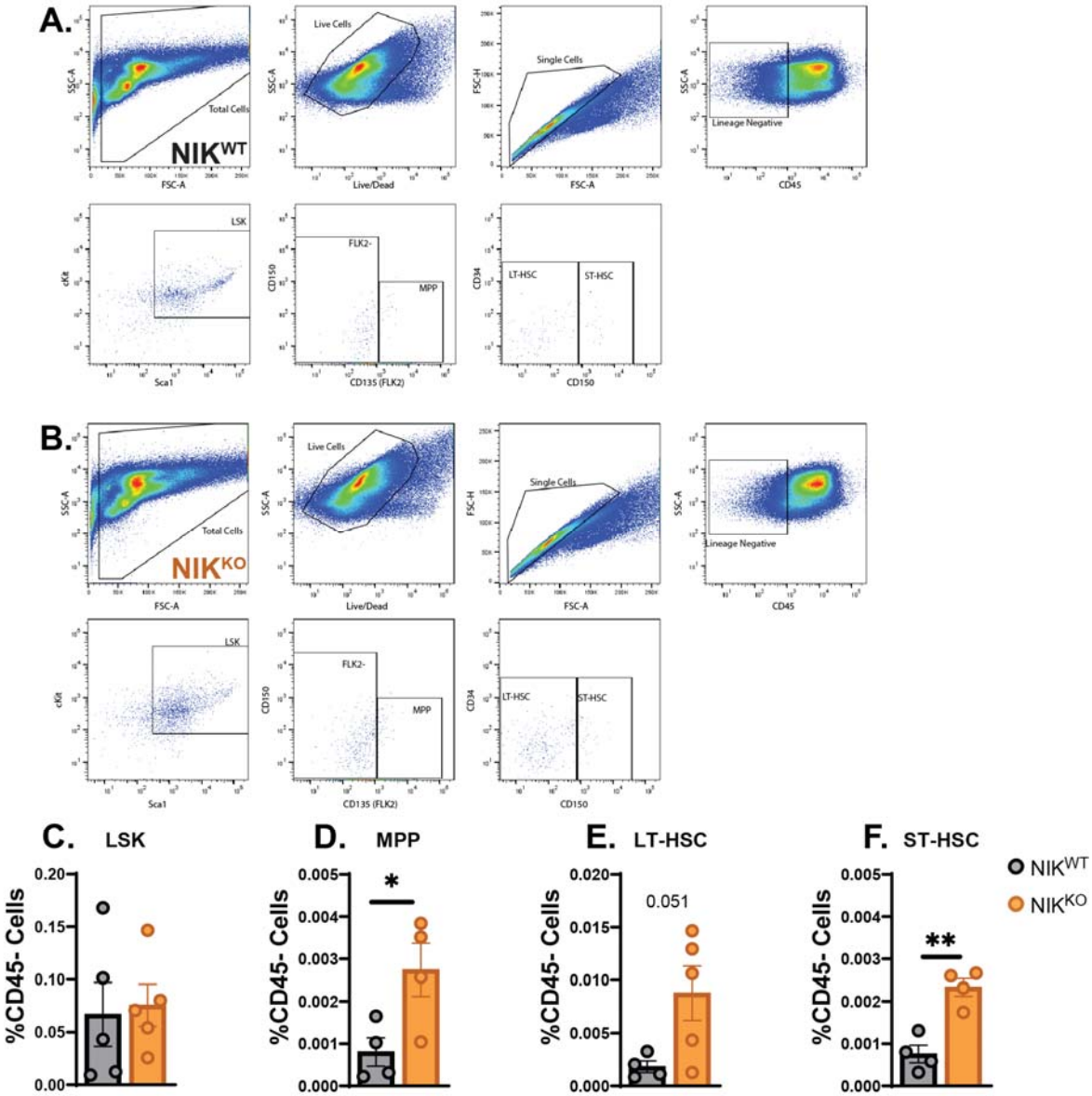

Supplemental Figure 3: Lineage negative bone marrow cells are enriched for low proliferative cells due to a loss of NIK. Gating scheme for stem cell analysis in WT **(A)** and NIK KO **(B)** bone marrow. Quantification of the stem cell compartment probing for differences in the LSK populations (early lymphoid progenitor) **(C)**, MPP (multi potent progenitor) **(D)**, LT-HSC (long term hemopoietic stem cell) **(E)**, and ST-HSC (short term hemopoietic stem cell) **(F)**

cell populations ($n \geq 4$ biological replicates). Statistics are a Student's T-test. *$p < 0.05$, **$p < 0.01$.

725 **Supplemental Table 1: Primary antibodies and antibody-based reagents used in the study.**

Catalog Number	Company	Reagent	Conjugate
Stemcell Panel			
A15423	Invitrogen	Anti-MO CD117/C-Kit	APC-Cy7
15-5981-81	Invitrogen	Anti-MO Ly-6A/E (SCA1)	PE-Cyn5
25-0481-80	Invitrogen	Anti-MO CD48	PE-Cyn7
12-1351-81	Invitrogen	Anti-MO CD135	PE
17-1502-80	Invitrogen	Anti-MO CD150	APC
11-0341-82	Invitrogen	Anti-MO CD34	FITC
Immune Panel			
25-0032-80	Invitrogen	Anti-MO CD3	PE-Cyn7
12-0452-81	Invitrogen	Anti-MO CD45R(B220)	PE
11-5931-81	Invitrogen	Anti-MO Ly-6G	FITC
35-0451-80	Invitrogen	Anti-MO CD45	PE-Cyn5.5
17-0112-81	Invitrogen	Anti-MO CD11b	APC
155505	Biolegend	Anti-MO Siglec F	PE
In vivo Polarization			
117351	Biolegend	Anti-MO CD11c	APC
144509	Biolegend	Anti-MO CD193 (CCR3)	FITC
123111	Biolegend	Anti-MO F4/80	PE-Cyn5
Blood and Spleen Immune Phenotyping			
25-0112-U100	Tonbo Biosciences	Anti-HU/MO M1/70 (CD11b)	APC-Cy7
115539	Biolegend	Anti-MO CD19	BV605
100267	Biolegend	Anti-MO CD3	APC-Fire810
65-4801-U100	Tonbo Biosciences	Anti-MO F4/80	PerCP-C5.5
128049	Biolegend	Anti-MO Ly6C	BV650
50-1276-U100	Tonbo Biosciences	Anti-MO Ly-6G	PE
107643	Biolegend	Anti-MO MHCII	BV711
506324	Biolegend	Anti-MO TNFα	PE-Cy7
13-0871-T100	Tonbo Biosciences	Viability	Ghost Dye 710
70-0161-U100	Tonbo Biosciences	Anti-MO CD16 / CD32 (Fc Shield) (2.4G2)	
ELISA Kit			
41-9234-P002	Tonbo Biosciences	Mouse IL-10 ELISA Matched Antibody Pair Kit	

Immunofluorescence			
MABT166	Millipore	Anti-TFAM	
CBL186	Millipore	Anti-DNA	
N-20	Santa Cruz Biotechnology	Anti-HSP60	
Western Blotting			
4994	Cell Signaling	Anti-NIK	
2697	Cell Signaling	Anti-pIKKα/IKKβ S176/180	
OP133	EMD Millipore	Anti-IKKα	
4882	Cell Signaling	Anti-p100/p52	
SC-365062	Santa Cruz Biotechnology	Anti-GAPDH	

Supplemental Table 2: Commercial reagents used in the study.

Catalog Number	Supplier	Reagent
L31963	Invitrogen	Violet Live/Dead dye
14-9161-71	Invitrogen	HU FCR Binding Inhibitor
M36008	Invitrogen	MitoSox
M22425	Invitrogen	Mitotracker Red FM
M7514	Invitrogen	Mitotracker Green FM
8778s	Cell Signaling	Mitotracker Deep Red FM
TLRL-PB5LPS	Invivogen	Ultrapure LPS-B5
214-14	PeproTech	Recombinant Murine IL-4
LS004174	Worthington Biochemical	Collagenase, Type 2
LS004186	Worthington Biochemical	Collagenase, Type 4
354234	Corning	Matrigel Basement Membrane Matrix
F3879	Sigma Aldrich	Fibrinogen
341584	Sigma Aldrich	Polyvinyl Alcohol
C35007	Invitrogen	CyQUANT
D275	Invitrogen	DiO
F3506	Sigma Aldrich	FMLP
TNB-0607-KIT	Tonbo Biosciences	Foxp3/Transcription Factor Staining Buffer Kit
75351	Sigma Aldrich	Oliogmycin A
15218	Cayman Chemical	FCCP
A8674	Sigma Aldrich	Antimycin A
ALX-350-360-G001	Enzo Life Sciences	Rotenone
1708891	BioRad	iScript
A25742	Universal SYBR Green	Invitrogen
700930	Cayman Chemical	MitoCheck Complex I Activity Assay Kit
700940	Cayman Chemical	MitoCheck Complex II Activity Assay Kit
700950	Cayman Chemical	MitoCheck Complex II/III Activity Assay Kit
700990	Cayman Chemical	MitoCheck Complex IV Activity Assay Kit
701000	Cayman Chemical	MitoCheck Complex V Activity Assay Kit
5120-0075	KPL	TMB Substrate
15702-10	Polysciences Inc	1um carboxylate microspheres - FITC

Supplemental Table 3: Oligonucleotides used in quantitative real-time PCR.

Name	Sequence
mCD163 F	CATCCGCCTTTGAATCCATCTCTTG
mCD163 R	CCTCCTCATTGTCTTCCTCCTGTG
mArg1 F	ACC TGG CCT TTG ATG TCC CTA
mArg1 R	AGA GAT GCT TCC AAC TGC CAG ACT
mRps 18 F	ACTTTTGGGGCCTTCGTGTC
mRps 18 R	GCCCAGAGACTCATTTCTTCTTG